BNL-65783

CONF-9806134--

# TRANSVERSE MOMENTUM DEPENDENT TWO-PION BOSE-EINSTEIN CORRELATIONS IN AU+AU COLLISIONS AT 11.6 A·GeV/$c$

J.H. Lee
*Physics Department, Brookhaven National Laboratory*
*Upton, NY 11973, USA*
*E-mail: jhlee@bnl.gov*

(for the E866 Collaboration)

Bose-Einstein correlations of $\pi^+\pi^+$ and $\pi^-\pi^-$ pairs collected by the BNL-E866 Forward Spectrometer in 11.6 A·GeV/$c$ Au + Au collisions have been measured. The data were analyzed using three-dimensional correlation functions parameterized by the Yano-Koonin-Potgoretskii and Bertsch-Pratt formalism to study transverse momentum dependent source parameters. Rapid decreases of longitudinal source radii and slower decreases in the transverse parameters with increasing transverse momentum were observed, which suggests a strong longitudinal and some transverse expansion. A freeze-out time $\tau_0$ was derived as $4.5 - 5$ fm/$c$, under the assumption of the freeze-out temperature $T = 130$ MeV, and the duration of emission was found to be $\delta\tau \approx 2 - 4$ fm/$c$.

## 1 Introduction

Bose-Einstein Correlation measurements are used to obtain the information on the space-time structure of the particle-emitting source in heavy ion collisions[1]. But the dynamical nature of collisions[2-6] complicated by the evolution of the system in the finite source lifetime limits the Bose-Einstein Correlation measurements only to the extent of space-time "region of homogeneity" from which bosons of similar momenta are emitted[6]. Correlation studies as a function of transverse momentum enable one to access more complete picture of the dynamical space-time structure of the source[6,7]. Recently much attention has been paid to the experimental measurements of transverse momentum dependent Bose-Einstein correlations, mainly at the CERN SPS energy[8,9,10]. In this contribution, we present results of the transverse momentum dependent source size measurements in Au+Au collisions at the AGS energy.

## 2 Experiment

The beam of 11.6 A·GeV/$c$ Au ions from the BNL Tandem-AGS complex was normally incident upon a Au target (1.5% or 3% of an interaction length), and the data were taken using the E866 Forward Spectrometer[11]. The Forward

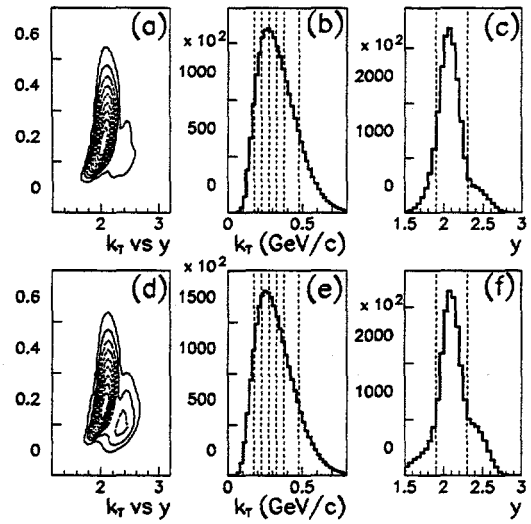


Figure 1: The distribution of the average transverse momentum ($K_T$) vs. the rapidity ($y$) and their projections for the $\pi^+\pi^+$ [(a,b,c)] and $\pi^-\pi^-$ [(d,e,f)] pairs. The dotted lines in the figures (b) and (e) represent the $k_T$ bins used in the analysis, and the dotted lines in the figures (c) and (f) show the rapidity regions selected.

Spectrometer was designed for handling the high multiplicity environment. It covers the forward rapidity region from 6 degrees to 28 degrees to the beam by rotating the spectrometer. It has a small aperture of about 5 msr, and consists of two dipole magnets, two tracking stations, and a Time-of-Flight (ToF) wall. The first magnet (M1) sweeps away low momentum particles, including delta rays, in order to reduce the hit multiplicity on the first tracking station which follows the M1. Each tracking station consists of a time projection chamber (TPC) sandwiched between a pair of projective drift chambers. Accurate and efficient track reconstruction is provided by pattern recognition in the two TPC's (TPC1 and TPC2) and fitting the tracks found in the TPC's with additional projected drift chamber hits to straight lines. If the two independently reconstructed straight tracks match inside the second magnet (M2), the momentum associated with the matched trajectory is obtained from the bending angle between the two tracks. After the momentum of the track is determined, the trajectory is projected toward the target through M1 to ensure the tracks originated from the target. Particle identification up to 4 GeV/$c$ for $\pi^{\pm}$ is obtained by the ToF hodoscope behind the second tracking station with 75 $p$sec timing resolution.

The data were taken in 1995. The total numbers of analyzed $\pi^+\pi^+$, $\pi^-\pi^-$, and $\pi^+\pi^-$ pairs are $1.5 \times 10^6$, $1.5 \times 10^6$, and $2.5 \times 10^6$, respectively. A large

## DISCLAIMER

fraction of the data comes from a single experimental setup: the Forward Spectrometer at 10 degrees, with magnetic fields of M1 and M2 −0.2 Tesla and +0.4 Tesla, respectively. This minimizes systematic uncertainties contributed by different experimental running conditions. The 30% ($\approx$ 1.65 barn) of the "minimum-biased" Au+Au cross section events corresponding to the most central collision gated by the New Multiplicity Array [12] were selected for the analysis. Fig. 1 shows the rapidity, $y$, and the average transverse momentum, $K_T$, distributions for $\pi^+\pi^+$ and $\pi^-\pi^-$ pairs. The $K_T$ used for the analysis is from 0.175 GeV/$c$ to 0.475 GeV/$c$ in 5 bins, corresponding $< K_T >$ = 0.2, 0.25, 0.3, 0.35, and 0.425, respectively, as displayed in Fig. 1. The rapidity range of pairs was limited to $1.9 \leq y_{\pi\pi} \leq 2.3$ for this analysis. The mid-rapidity is $y_{\rm CMS} = 1.6$.

## 3 Correlation Function Parameterization

The correlation function $C_2$ is the ratio of the two-particle probability to the product of the single-particle probabilities for particles with momenta $\boldsymbol{p_i}$. Experimentally it is given by the normalized ratio of the number of correlated (signal) pairs $S$ to the number of uncorrelated (background) pairs $B$:

$$C_2(\boldsymbol{q}, \boldsymbol{K}) = \frac{P(\boldsymbol{p}_1, \boldsymbol{p}_2)}{P(\boldsymbol{p}_1)P(\boldsymbol{p}_2)} = \mathcal{N} \cdot \frac{S}{B \cdot w_{Coulomb}}\,, \qquad (1)$$

where $(q_0, \boldsymbol{q}) = (E_1 - E_2, \boldsymbol{p}_1 - \boldsymbol{p}_2)$ and $\boldsymbol{K} = \frac{\boldsymbol{p}_1 + \boldsymbol{p}_2}{2}$ denote the relative and average momentum of the pair, respectively.

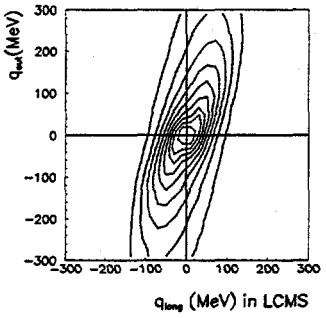


Figure 2: Contour plot of the correlation of $q_{out} - q_{long}$ for $\pi^-\pi^-$. The $\pi^+\pi^+$ plot looks similar.

The signal pairs are from the same events and the background pairs are obtained by mixing different events with the same experimental condition. The background pairs were constructed with 20 times more statistics than the number of correlated pairs, and weighted with the Coulomb factor $w_{Coulomb}$ to remove the correlation created by the Coulomb effect in the correlated pairs. To compare with other published results[13,14], the one-dimensional correlation functions for $\pi^+\pi^+$ and $\pi^-\pi^-$ were parameterized by,

$$C_2(Q_{inv}) = \mathcal{N}(1 + \lambda e^{-R_{inv}^2 Q_{inv}^2}), \qquad (2)$$

where the Lorentz invariant variable $Q_{inv}^2$ is defined as $q_0^2 - \boldsymbol{q}^2$.

For the three-dimensional parameterization, the data were fit with the Yano-Koonin-Potgoretskii (YKP) [6,15,16] scheme which is a function of the space-time components $(R_\perp, R_\parallel, R_0)$ and the average longitudinal velocity $v$:

$$C_2(\boldsymbol{q},\boldsymbol{K}) = \mathcal{N}[1 + \lambda e^{-R_\perp^2(\boldsymbol{K})q_\perp^2 - R_\parallel^2(\boldsymbol{K})(q_\parallel^2 - q_0^2) - (R_0^2(\boldsymbol{K}) + R_\parallel^2(\boldsymbol{K}))(q\cdot U(\boldsymbol{K}))^2}]. \quad (3)$$

Here $q_\perp = \sqrt{q_{side}^2 + q_{out}^2}$ and $q_\parallel$ is the longitudinal component. The four-velocity $U$ only has a longitudinal spatial component:

$$U(\boldsymbol{K}) = \gamma(\boldsymbol{K})(1,0,0,v(\boldsymbol{K})), \text{ with } \gamma = \frac{1}{\sqrt{1-v^2}}. \quad (4)$$

The data have been also parameterized with the Bertsch-Pratt (BP) Cartesian decomposition [2,17]:

$$C_2(\boldsymbol{q},\boldsymbol{K}) = \mathcal{N}[1+\lambda e^{-R_{long}^2(\boldsymbol{K})q_{long}^2 - R_{side}^2(\boldsymbol{K})q_{side}^2 - R_{out}^2(\boldsymbol{K})q_{out}^2 - 2R_{out,long}^2(\boldsymbol{K})q_{out}q_{long}}] \quad (5)$$

where $\lambda$ is a chaoticity parameter, with $\lambda$=0 corresponding to a totally coherent and $\lambda$=1 corresponding to a totally chaotic source. The longitudinal component of $\boldsymbol{q}$, $q_{long}$ is parallel to the beam, $q_{side}$ is perpendicular both to the beam and to the average momentum, and $q_{out}$ is orthogonal to $q_{side}$ and $q_{long}$. The source radius parameters $R_{long}$, $R_{side}$, and $R_{out}$ correspond to three dimensional radius parameters in the ($q_{long}$,$q_{side}$,$q_{out}$) space. The "out-longitudinal" cross term [18] $R_{out,long}^2$, which can be either positive or negative, is included in the function to accommodate the rotation of the $q_{out}$-$q_{long}$ plane as seen in Fig. 2. The correlation functions, Eq. 3 and Eq. 5, are evaluated in the Longitudinally Co-Moving System (LCMS), which is the longitudinally boosted frame where the average pair momentum $\boldsymbol{K}$ has no longitudinal component, $\beta_L = 0$.

## 4 Analysis

The $\boldsymbol{q}$ resolution functions calculated from the Monte-Carlo simulations of the detector system using GEANT [19] and the data reconstruction chain are shown in Fig. 3. The resolution factors contribute to an underestimation of the source parameters. The systematic uncertainties of the fitted radius parameter are estimated to be less than 10%. No correction for this effect has been applied to the data.

A minimum separation of 1 cm between two tracks at the middle planes of TPC1 (2.4 m from the target) and TPC2 (3.8 m from the target) in both

the $x$ and $y$ directions is applied in order to exclude regions of inefficient track reconstruction. The same condition for the minimum track separation is applied in the selection of mixed events to prevent introducing any bias from the cut.

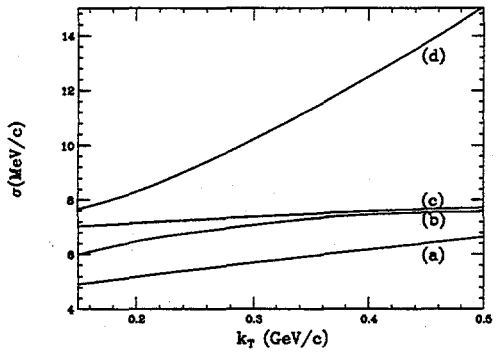


Figure 3: Resolution functions of the $q$ components, obtained by averaging over the other $q$ components, are shown as a function of $K_T$ for $Q_{inv}$ [(a)], $q_{long}$ [(b)] in LCMS, $q_{side}$ [(c)], and $q_{out}$ [(d)].

The final state Coulomb interaction between two pions is corrected for by an iterative method which takes into account the pion source size [14] and the momentum resolution. Fig. 4 shows Coulomb correction factors for two pions with and without the momentum resolution smearing. For the comparison, the Gamov function which assumes a point-like source is also displayed in the figure. To test the quality of the Coulomb corrections, the correction functions are applied to $\pi^+\pi^-$ correlations which is dominated by the mutual Coulomb interactions for small $q$. It is demonstrated in Fig. 5 that the $\pi^+\pi^-$ correction function becomes close to unity after applying the Coulomb correction function calculated for a finite source and folded with the experimental momentum resolutions. No correction is applied for Coulomb effects between the pair and the remaining particles.

Fitting the data to the correlation functions was done by minimizing the logarithm of the likelihood function:

$$-\ln \mathcal{L} = \sum_{i}^{n} [C_i B_i - S_i \ln(C_i B_i) + \ln(S_i!)], \tag{6}$$

where $C_i$ is the correlation function, and $S_i$ is the number of signal counts in the $i$-th three dimensional $q$ bin, and $B_i$ is the number of background events weighted by a Coulomb factor in the bin. The minimization is done using MINUIT [20]. The projections of the $\pi^+\pi^+$ correlations and of the fits for the YKP and BP parameterizations, obtained by averaging over the two other components of $-50 < q < 50$ MeV/$c$ weighted by the number of background pairs, are plotted in Figs. 6 and 7. The fits reproduce the data for all bins in $K_T$, and for both parameterizations.

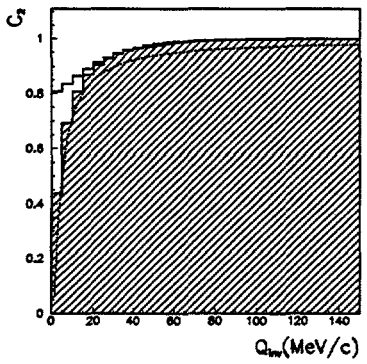


Figure 4: Coulomb correction functions without (shaded distribution) and with (unshaded) momentum resolution. The Gamov function is shown as a dotted curve.

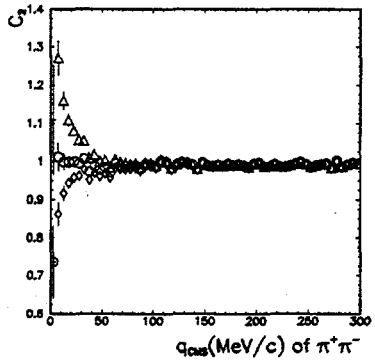


Figure 5: $\pi^+\pi^-$ correlation functions $C_2$ as a function of $|q|$ (in CMS system): The raw correlation ($\triangle$), correlations corrected with the Coulomb function ($\diamond$) and corrected for Coulomb and momentum resolution ($\bigcirc$) are shown.

## 5 Results

The fitted values from the one dimensional parameterization of Eq. 2 are $R_{inv}$ = 5.69 ± 0.09, $\lambda$ = 0.47 ± 0.01 for $\pi^+\pi^+$ and $R_{inv}$ = 6.12 ± 0.09, $\lambda$ = 0.48 ± 0.01 for $\pi^-\pi^-$. The difference in the size between $\pi^+\pi^+$ and $\pi^-\pi^-$ sources may be attributed to the Coulomb interaction between each of the pions and the rest of the system. With the simplified assumption [21] that the Coulomb field of the rest of the system can be described by a central Coulomb potential with an effective charge $Z_{eff}$, the difference in the source size results in $Z_{eff} \approx 40$.

Multi-dimensional radius parameters for the five $K_T$ bins are shown in Fig. 9 for the YKP parameterization, and for the BP parameterization in Fig. 10. The fitted regions for each points are indicated by lines in the horizontal direction. Fitted $\lambda$ parameters for both parameterizations are shown in Fig. 11. The longitudinal component $R_\parallel$ (and $R_{long}$) features a clear $K_T$ dependence. Since the slope of the decrease is expected to grow with the expansion rate of the source [3,7,22,23], it can be interpreted as an indication of a longitudinal expansion of the source before freeze-out. To quantify this systematic decrease, $R_\parallel$ values are fit with $R_\parallel \propto 1/m_T^\alpha$, where $m_T = \sqrt{K_T^2 + m_\pi^2}$, since the approximate analytic "$m_T$ scaling" ($R_\parallel \propto 1/\sqrt{m_T}$) from the hydrodynamical models [3,22] has been commonly used as a basis for experimental

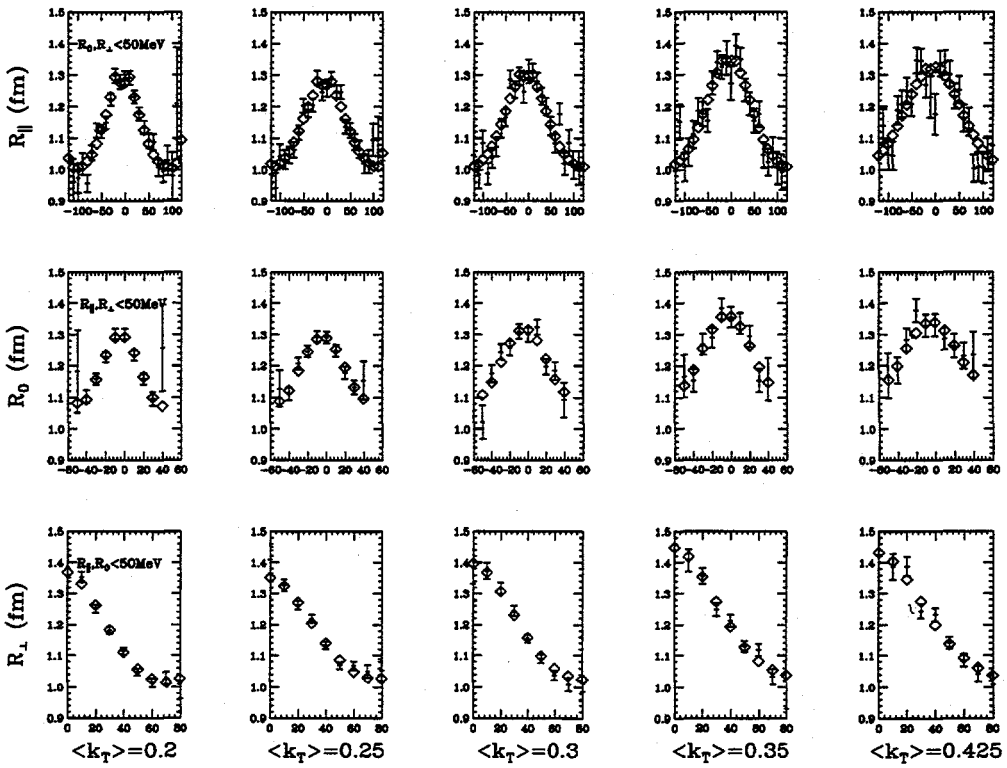


Figure 6: Projections of the $\pi^+\pi^+$ correlation function and the three dimensional fit using the YKP parameterization. The first, second, and third rows correspond for $R_{\parallel}$, $R_0$, and $R_{\perp}$ and the each column represents bins in $K_T$. The data are shown with statistical error bars and the projections of the correlation functions are displayed with symbols ($\diamond$).

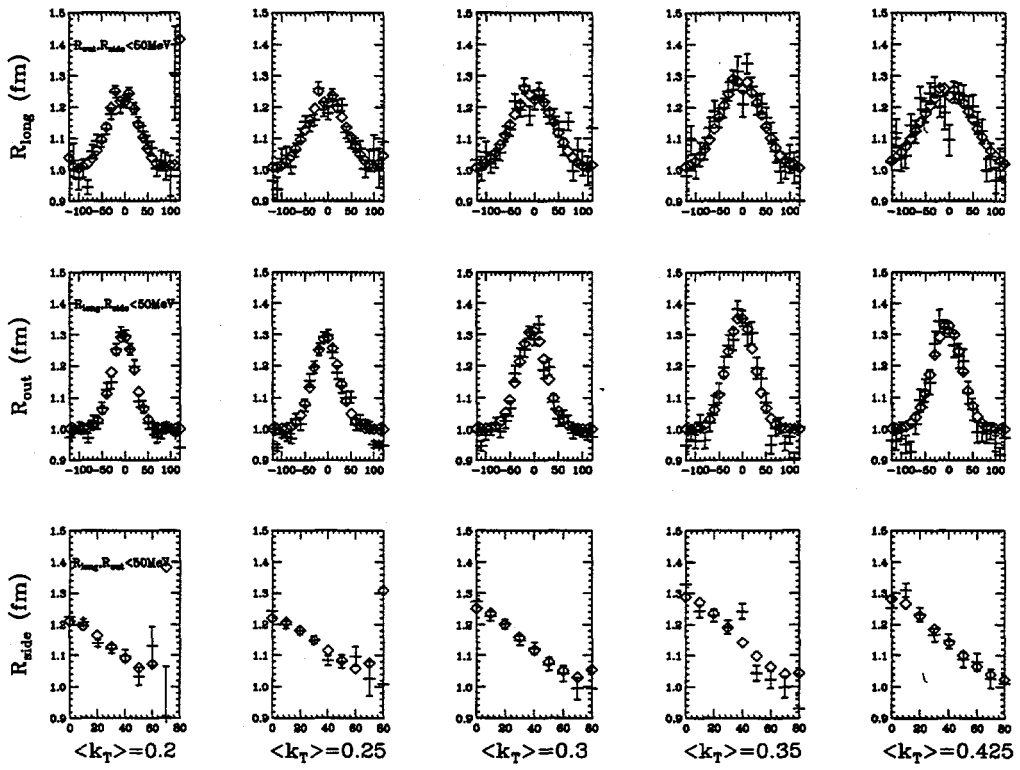


Figure 7: Projections of the $\pi^+\pi^+$ correlation function and the three dimensional fit using the BP parameterization. The first, second, and third rows correspond for $R_{long}$, $R_{out}$, and $R_{side}$ and the each column represents bins in $K_T$. The data are shown with statistical error bars and the projections of the correlation functions are displayed with symbols ($\diamond$).

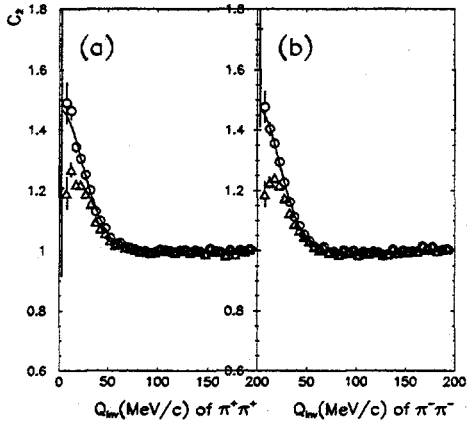


Figure 8: One-dimensional $\pi^+\pi^+$ [(a)] and $\pi^-\pi^-$ [(b)] correlation function $C_2(Q_{inv})$. The raw correlation function is shown with triangles ($\triangle$) and the Coulomb function corrected one is shown with circles ($\bigcirc$).

and theoretical characterization of the dependence of the source radii on the transverse momentum. Fitted exponent $\alpha$ values for $R_{\parallel}$ in Fig. 9 are $0.75 \pm 0.04$ (with $\chi^2 = 1.4$) for $\pi^+\pi^+$, and $0.57 \pm 0.09$ ($\chi^2 = 0.29$) for $\pi^-\pi^-$, which indicates that the $K_T$-dependence of $R_{\parallel}$ is similar with or stronger than the $1/\sqrt{m_T}$ behavior.

The values of $R_{\perp}$ show a weaker and less clear $K_T$-dependency compared to $R_{\parallel}$. Fitting $R_{\perp}$ to $1/m_T^{\alpha}$ for a quantitative comparison with $R_{\parallel}$ results in $\alpha = 0.26 \pm 0.07$ ($\chi^2 = 0.7$) for $\pi^+\pi^+$, and $0.15 \pm 0.08$ ($\chi^2 = 2.0$) for $\pi^-\pi^-$. This can support the interpretation that the source undergoes some transverse expansion [23] as well as longitudinal expansion. The geometrical source parameter value $R_{\perp} \approx 4.5$ fm at small $K_T$ corresponds to r.m.s. radius of $r_{\rm r.m.s.} = \sqrt{3}R_{\perp} \approx 7.8$ fm to be compared with an r.m.s. radius of Au nuclei measured by electron scattering [24] of 5.33 fm. The $r_{\rm r.m.s.}$ values from the correlation measurement give larger radii than the Au r.m.s. radius. The difference can be understood as a transverse expansion contribution [6] to the geometrical radius $R_{\perp}$. The source sizes differences between $\pi^+\pi^+$ and $\pi^-\pi^-$ are only apparent for the $R_{\perp}$ dimension, which qualitatively agrees with nuclear Coulomb field effects [25]. The $R_{\perp}$ values show a reasonable overall agreement with $R_{side}$ within systematic uncertainties. The rapidity of YKP frame ($y_{YKP} = \frac{1}{2}\ln\frac{1+v}{1-v} \approx -0.3$) appears to be slower than the LCMS, which can be understood as an

effect of the thermal smearing of the pion velocities in the source[23].

One can derive an estimate of the approximate average freeze-out time $\tau_0$ by assuming a purely longitudinally expanding system without transverse flow from[3,22]:

$$R_{\parallel} = \tau_0 \sqrt{\frac{T}{m_T}}, \tag{7}$$

where $T$ is a freeze-out temperature. By assuming[26] $T = 130$ MeV, the freeze-out time is $\tau_0 \approx 5$ fm/$c$ at $< K_T > = 200$ MeV/$c$, and $\tau_0 \approx 4.5$ fm/$c$ at $< K_T > = 400$ MeV/$c$.

An estimate of the phase of freeze-out, i.e., duration of the particle emission, $\delta\tau$ can be provided by the temporal parameter $R_0$, or can be obtained[5] from the difference of $R^2_{out}$ and $R^2_{side}$ from the BP parameterization,

$$\delta\tau = \frac{1}{\beta_\perp} \sqrt{R^2_{out} - R^2_{side}}, \tag{8}$$

where $\beta_\perp$ is the transverse velocity of the pair. The durations of emission given by both parameterizations are $\delta\tau \approx 2 - 4$ fm/$c$ showing $\delta\tau \lesssim R_\perp$. That excludes the possibility of a long-lived state created from a phase transition[27] at the AGS energy. It is shown that the $\delta\tau$ values for $\pi^+\pi^+$ are larger than for $\pi^-\pi^-$, and they increase at small $K_T$ for both $\pi^+\pi^+$ and $\pi^-\pi^-$. Those systematic features of the effective lifetime are consistent with both parameterizations within the systematic uncertainties as shown in Fig. 12.

## 6 Summary

Preliminary results on the transverse momentum dependent source size measurement for $\pi^+\pi^+$ and $\pi^-\pi^-$ in Au+Au collisions using the E866 Forward Spectrometer at the AGS have been presented. Multi-dimensional Bose-Einstein correlation functions parameterized by the Yano-Koonin-Potgoretskii method show a rapid decrease of $R_{\parallel}$ and a slower and less clear decrease of $R_\perp$ as the transverse momentum increases. This may indicate a strong longitudinal and a moderate transverse expansion before freeze-out. An approximate freeze-out time was estimated as $\tau_0 \approx 4.5 - 5$ fm/$c$ with the duration of emission $\delta\tau \approx 2 - 4$ fm/$c$. These results agrees a Bertsch-Pratt parameterization within the systematic uncertainties. The data indicate systematic differences in the source parameters between $\pi^+\pi^+$ and $\pi^-\pi^-$. The $\pi^-$ source has a larger transverse size, smaller $K_T$ dependence, and smaller duration of emission. This may be explained by the Coulomb interaction between pions and nucleons, but to clarify the effects, further theoretical and experimental investigation are needed.

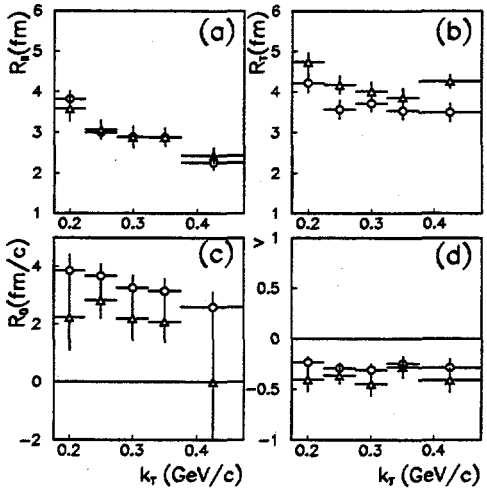


Figure 9: Fitted radius parameters for the YKP parameterization for $R_{\parallel}$ [(a)], $R_{\perp}$ [(b)], $R_0$ [(c)], and $v$ [(d)]. Circles (○) shown for $\pi^+\pi^+$ and triangles (△) for $\pi^-\pi^-$. The error bars are statistical only.

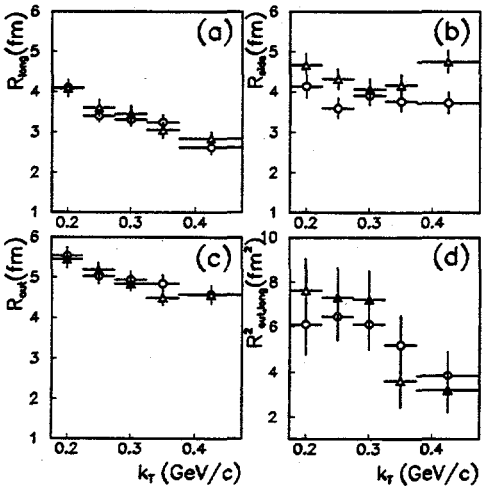


Figure 10: Fitted radius parameters for the BP parameterization for $R_{long}$ [(a)], $R_{side}$ [(b)], $R_{out}$ [(c)], and $R_{out,long}$ [(d)]. Circles (○) shown for $\pi^+\pi^+$ and triangles (△) for $\pi^-\pi^-$. The error bars are statistical only.

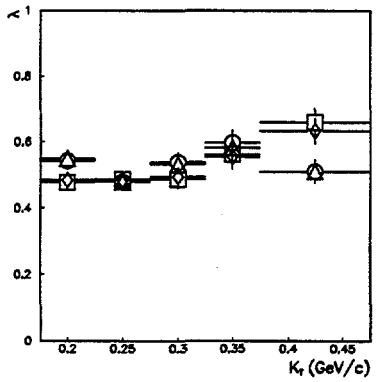


Figure 11: $\lambda$ parameters for the YKP parameterization ($\triangle$: $\pi^+\pi^+$, $\diamond$: $\pi^-\pi^-$) and the BP parameterization ($\bigcirc$: $\pi^+\pi^+$, $\square$: $\pi^-\pi^-$).

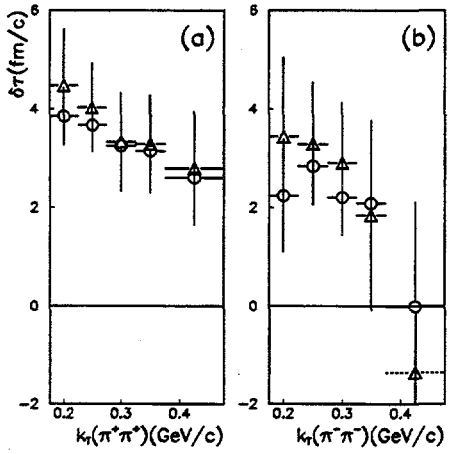


Figure 12: $\delta\tau$ calculated from the BP parameterization for $\pi^+\pi^+$ [(a)] and $\pi^-\pi^-$ [(b)] as functions of $K_T$ are shown with triangles ($\triangle$). For the last point with dotted a line in the (b) panel, where $R_{side} > R_{out}$, an absolute value has taken in the square root in Eq. 8. For a comparison, $R_0$ values from YKP parameterization are also shown in the figures with circles ($\bigcirc$).

**Acknowledgments**

This work was supported by the U.S. Department of Energy under contracts with BNL (DE-AC02-98CH10886), Columbia University (DE-FG02-86-ER40281), LLNL (W-7405-ENG-48), MIT (DE-AC02-76ER03069), UC Riverside (DE-FG03-86ER40271), and by NASA (NGR-05-003-513), under contract with the University of California, and by Ministry of Education and KOSEF in Korea, and by the Ministry of Education, Science, and Culture of Japan.

**References**

1. See D.H. Boal, C.G. Gelbke, and B. Jennings, *Rev. Mod. Phys.* **62**, 553 (1990) for a review.
2. S. Pratt, *Phys. Rev.* D **33**, 1314 (1986).
3. A.N. Makhlin and Yu.M. Sinyukov, *Z. Phys.* C **39**, 69 (1988).
4. T. Csörgő and B. Lörstad, *Phys. Rev.* C **54**, 1390 (1996).
5. H. Heiselberg, *Phys. Lett.* B **379**, 27 (1996).
6. U. Heinz, contribution to this volume.
7. U.A. Wiedemann, P. Scotto, and U. Heinz, *Phys. Rev.* C **53**, 918 (1996).
8. J. Sullivan, contribution to this volume.
9. R. Ganz, contribution to this volume.
10. H. Appelshäuser *et al.*, *Eur. Phy. J.* C **2**, 661 (1998).
11. H. Sako, Ph.D. Thesis, University of Tokyo, INS-J-186 (1997).
12. L. Ahle, Ph.D. Thesis, MIT (1997).
13. J. Barrett *et al.*, *Phys. Rev. Lett.* **78**, 2916 (1997).
14. M. Baker *et al.*, *Nucl. Phys.* A **610**, 213c (1996).
15. F. Yano and S. Koonin, *Phys. Lett.* B **78**, 556 (1978).
16. S. Chapman, J.R. Nix and U. Heinz, *Phys. Rev.* C **52**, 2694 (1995).
17. G. Bertsch, *Nucl. Phys.* A **498**, 173c (1989).
18. S. Chapman, P. Scotto and U. Heinz, *Nucl. Phys.* B **52**, 2694 (1995).
19. CERN Computing Division, CERN Program Library Long Writeup W5013.
20. F. James, CERN Program Library Long Writeup D506.
21. G. Baym and P. Braun-Munzinger, *Nucl. Phys.* A **610**, 286c (1996).
22. J. Bolz *et al.*, *Phys. Lett.* B **300**, 404 (1993).
23. Wu Y.-F. *et al.*, *Eur. Phy. J.* C **1**, 599 (1998).
24. M.A. Preston and R.K. Bhaduri, *Structure of the Nucleus*, p.99, Addison-Wesley, Massachusetts (1975).
25. H.W. Barz, contribution to this volume.
26. J. Stachel, *Nucl. Phys.* A **610**, 509c (1996).
27. D.H. Rischke and M. Gyulassy, *Nucl. Phys.* A **608**, 479 (1996).